ACS APPLIED MATERIALS & INTERFACES

www.acsami.org Research Article

Influence of Electrolyte Saturation on the Performance of Li−O_2 Batteries

Amirhossein Sarabandi, Andre Adam, and Xianglin Li*

Cite This: *ACS Appl. Mater. Interfaces* 2024, 16, 62902−62913 Read Online

ACCESS | Metrics & More | Article Recommendations | Supporting Information

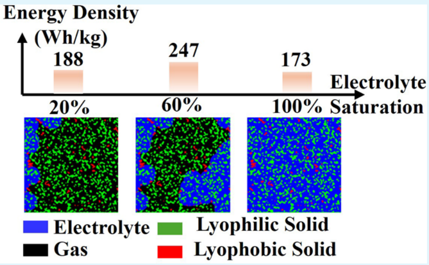

ABSTRACT: Electrolyte saturation can strongly affect the Li−O_2 battery performance. However, it is unclear to what extent saturation reduction will impact the battery capacity. In this study, we investigated the influence of electrolyte saturation and distribution within a porous positive electrode on the deep discharge−charge capacities and cycling stability. The study used both models and experiments to investigate the change of electrolyte distribution, double-layer capacitance, ohmic resistance, and O_2 concentration in the positive electrode at different electrolyte saturations. Results revealed that electrodes with 60% electrolyte saturation achieved almost the same maximum discharge (6.38 vs 6.76 mAh/cm^2) and charge (5.52 vs 5.65 mAh/cm^2) capacities with fully saturated electrodes. The partially wet positive electrode (40% saturation) obtained more cycles than the electrode with 100% saturation before the discharge capacity dropped below the cutoff point. However, the electrode with 40% saturation had a low average charging efficiency of 88.76%, whereas the fully saturated electrode obtained 98.96% charging efficiency. Moreover, the fully wet positive electrode had the lowest overpotential during cycling (1.26−1.39 V). The measured electrochemically active surface areas showed that even 40% saturation could sufficiently wet the positive electrode surface and obtain a double-layer capacitance (18.12 mF) similar to that with 100% saturation (20.4 mF). Furthermore, a considerable increase in O_2 concentration at wetted surface areas was observed for the electrolyte saturation of less than 60% due to the significantly higher O_2 diffusivity in the gas phase.

KEYWORDS: *lithium oxygen battery, deep discharge capacity, cycling stability, electrolyte distribution, electrolyte saturation, double-layer capacitance, oxygen concentration*

1. INTRODUCTION

Lithium−oxygen (Li−O_2) batteries have attracted significant attention due to their potential to have high energy densities, which theoretically can surpass lithium-ion ones.[1,2] The battery consisted of lithium metal as the negative electrode, a separator fully wet with electrolyte, and a carbon-based porous positive electrode. In the discharge process, the Li metal is oxidized in the negative electrode to produce lithium ions, transferring through the electrolyte and reaching the positive electrode surface areas, which is shown in eq 1. As it is depicted in eq 2, the solid discharge product, Li_2O_2, is produced from the reaction between Li^+ and O_2 in the positive electrode by the oxygen reduction reaction (ORR).[3] Li_2O_2 is decomposed in the charging process through the oxygen evolution reaction (OER) and generates oxygen and Li ions on the positive electrode side. The overall electrochemical reaction in the negative and positive electrodes is shown in eq 3.[4]

$$\text{negative:}\quad \mathrm{Li} \underset{\text{charge}}{\overset{\text{discharge}}{\rightleftharpoons}} \mathrm{Li}^+ + e^- \tag{1}$$

$$\text{positive:}\quad \mathrm{O_2} + 2e^- + 2\mathrm{Li}^+ \underset{\text{charge}}{\overset{\text{discharge}}{\rightleftharpoons}} \mathrm{Li_2O_2}\ (\text{solid}) \tag{2}$$

$$\text{overall:}\quad 2\mathrm{Li} + \mathrm{O_2} \underset{\text{charge}}{\overset{\text{discharge}}{\rightleftharpoons}} \mathrm{Li_2O_2}\ (\text{solid}) \tag{3}$$

The Li−O_2 batteries using nonaqueous electrolytes can provide relatively high charging and discharging efficiency[5] and will be used in this work. The electrochemical performances of Li−O_2 are dictated by mass transfer in porous electrodes, which is complicated because of the wide range of pore size distribution, irregular pore shapes, and gas-trapped regions in pore spaces.[6,7] Since the diffusivity of O_2 in the gas phase is several orders of magnitude higher than in the liquid phase, the filling liquid electrolyte determines the effective transport characteristics.[8] Due to the slow O_2 dissolution into the electrolyte and slow mass transfer in the liquid, researchers have studied the impact of the electrolyte amount, partially and flooded electrodes, on Li−O_2 battery performance. Xia et al.[9] demonstrated that a partially wetted positive electrode can

Received: July 22, 2024
Revised: October 12, 2024
Accepted: October 21, 2024
Published: November 4, 2024

https://doi.org/10.1021/acsami.4c12168
ACS Appl. Mater. Interfaces 2024, 16, 62902−62913

increase the discharge capacity by 60% and rate capability by 1 order of magnitude compared to a flooded positive electrode. This is mainly attributed to the nonuniform deposition of Li_2O_2 and incomplete utilization of positive electrode volume due to insufficient oxygen solubility and diffusivity in the electrolyte. Xu et al.[10] showed that the amount of electrolyte added to Li−air batteries affected discharge performance. While the optimum amount of electrolyte may vary depending on the positive electrode type, the maximum capacity and specific energy were obtained with 135 μL of electrolyte (which varied between 50 and 200 μL) for the positive electrode with a very low mesoporous volume.

Given that studying the effect of pore structure, discharge product distribution, and the concentration of the O_2 on Li−O_2 performance is challenging through experiments, a group of researchers have used modeling to investigate these factors. Li et al.[11] performed a modeling on oxygen effective diffusivity and electrical conductivity and an experiment on deep discharge capacity at different electrolyte saturations of a Li−air battery. It was shown that the 60% saturation level was the optimum electrolyte saturation, regarding the highest specific capacity (5034.1 mAh/g) and electrical conductivity of around 100 S/m. Wang and Hao[12] performed a simulation to investigate the capacity of Li−O_2 batteries with different electrolyte filling modes, including flooded and partially wetted positive electrodes. It was revealed that the discharge capacity and voltage of a partially wetted positive electrode are 3.7 and 0.4 V higher than those of a flooded one. It resulted from better O_2 diffusion through a partially wet positive electrode. A similar work carried out by Wang and Li[13] performed a pore-scale simulation to evaluate Li−O_2 batteries' specific capacity at different levels of electrolyte saturation. They obtained maximum and minimum capacities at saturation levels of 84.7 and 100%, respectively. Mayur and Bessler[14] also developed a 2D multiphysics model to study the effect of electrolyte saturation on Li−air batteries' overpotential and current density. It was revealed that the battery with high electrolyte saturations, more than 90%, had a lower overpotential under low current density. In the high current density region, which had a higher consumption of O_2, cells with low electrolyte saturation performed better. The distribution of solid discharge products can play a critical role in Li−O_2 performance since they can clog the pore throats and consequently prevent O_2 from reaching reaction sites. A 3D transient model developed by Gwak and Ju[15] showed that the cell performance was poor at very low and high electrolyte saturation since the solid discharge products (Li_2O_2) were distributed more uniformly within the partially wetted positive electrodes compared to the flooded ones.

Some researchers studied the electrolyte volume effect on battery performance. Xiao et al.[16] varied the electrolyte amount between 100 and 150 μL in air electrodes of Li−air batteries made from Ketjen black with a specific pore volume of 7.65 cm^3/g. The specific capacity increased considerably by increasing the electrolyte volume from 100 to 150 μL, which was attributed to the large volume expansion of the cathode. The effect of pore volume and electrolyte saturation on Li−O_2 battery performance was also studied by Saengkaew et al.[17] They demonstrated that the positive electrodes that had relatively large pore volumes, such as KB-based electrodes, showed reduced performance at the electrolyte injection ratios of 80 and 60%, leading to a lower cycle life than the electrode with 100% electrolyte. It was because of the additional electrolyte amounts required to wet the surface of the electrodes with large pore volumes.

Electrolyte distribution within a porous positive electrode is usually heterogeneous due to gas entrapment through pore spaces.[18] Therefore, it is important to have a more uniform electrolyte distribution since it affects the distribution of the solid discharge products. Decreasing the amount of electrolyte to a limited condition called lean electrolyte makes the electrolyte distribution even more heterogeneous. This limited amount of electrolyte causes the significant movement of electrolytes with the formation/decomposition of discharge products within the porous positive electrode.[19] In this regard, Matsuda et al. studied an electrolyte injection technology[20] and revealed the stamping method using two highly hydrophilic filters as electrolyte transfer agents could lead to a uniform 2D distribution of electrolytes over the positive electrode surface. It was also shown that for electrolyte loading less than 100%, the inhomogeneous electrolyte distribution decreased the effective electrochemical surface, leading to an increase in overpotential during cycling. A study conducted by Ono et al.[21] revealed that the reason for the poor cycling performance of Li−O_2 batteries under lean electrolyte and high-areal capacity conditions was not because of the limited amount of electrolyte. The study showed that even adding the same electrolyte amount as the lost amount did not make the battery cycle longer since the decomposition of solid-state side products caused carbon electrode degradation and finally battery failure.

Energy density is one of the most important parameters that should be considered for Li−O_2 batteries. To achieve higher energy densities, the weight of cell components should be minimized as much as possible.[22] Employing positive electrodes with partial wetting conditions is an approach that can reduce the weight of the internal components. The influence of electrolyte injection ratio in the porous carbon electrode on energy density was studied by Matsuda et al.[23] They found that the ratio of electrolyte amount to battery capacity should be less than 10 g/Ah to develop batteries with an energy density of more than 300 Wh/kg. They also used modeling to show that the energy density of Li−O_2 batteries increased by decreasing the electrolyte injection ratio from 100 to 40%. The effect of lean electrolyte conditions on the energy density of Li−air batteries was studied by Matsuda.[24] It was revealed that the battery could achieve comparable energy density to Li-ion batteries with electrolyte amount ($<20\ \mu L/cm^2$) and high-areal capacity ($>2\ mAh/cm^2$).

According to the above studies, there is evidence that the electrolyte amount can play a crucial role in overall Li−O_2 battery performance and cycle life. However, it is still unclear how spatial distributions of electrolytes affect the concentration of the O_2 at the wetted surface of the electrode, electrochemically active surface areas, and ohmic resistance within the positive electrode. These factors, in turn, have a significant impact on deep discharge−charge capacities and cycling stability. To fill this knowledge gap, first, we developed a pore morphology model to visualize the heterogeneous electrolyte distribution within porous positive electrodes. The wettability distribution within the positive electrode was determined by the binder fraction, discussed in EDX analysis of the microporous layer (MPL) in the Supporting Information (SI) and depicted in Figure S5 as well, to study the wetting behavior of the electrode on electrolyte distribution. We used the electrolyte distribution to calculate

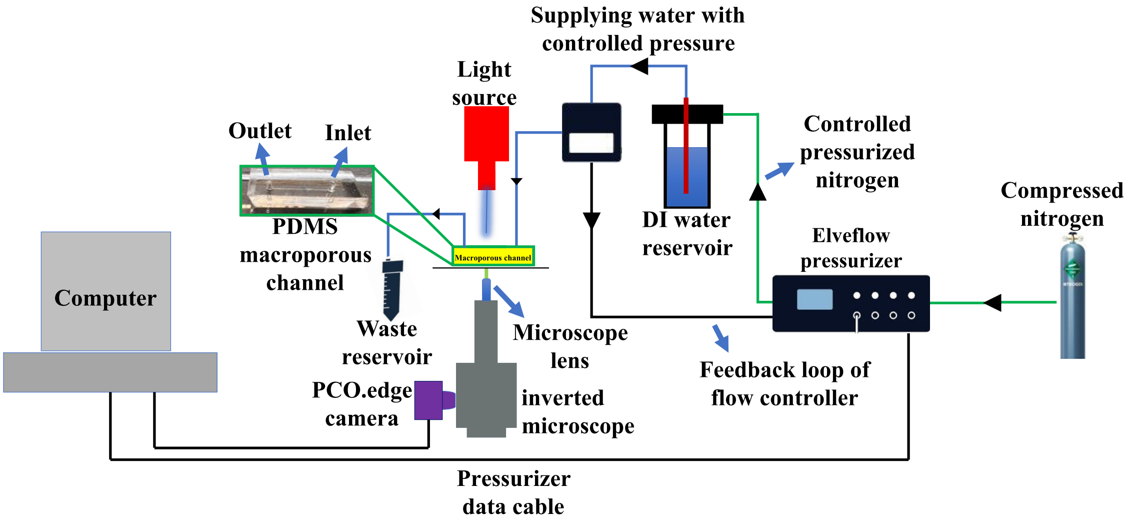

Figure 1. Schematic of the experimental setup used for the capillary−saturation experiment.

the O_2 concentration at the wetted surface of the electrode and the effective diffusivity of the cathode, as well. Second, we conducted experiments to investigate the effect of electrolyte saturation on positive electrode internal wettability, ohmic resistance, maximum discharge and charge capacities, and cycling performance at a given capacity.

2. MODELING

2.1. Electrolyte Distribution. We developed a computationally efficient pore morphology model to simulate the heterogeneity of electrolyte distribution within a porous positive electrode considering the geometry of a pore structure. In porous media with irregular pores, pore throats with different diameters result in different local capillary pressures in the presence of a liquid−gas interface at the pore throats. This local capillary pressure was used to determine whether a meniscus could go through a pore throat with a specific diameter.

If the liquid within porous media has a contact angle of less than 90°, the local capillary pressure in eq 4 assists the liquid in proceeding through pore throats. In contrast, for a lyophobic case, the capillary pressure acts as a resistance to the liquid to move through pore throats.

$$\Delta P_c = 2\gamma \cos\theta\left(\frac{1}{d} + \frac{1}{2r}\right) \tag{4}$$

In eq 4, γ represents interfacial tension between the nonwetting and wetting phases, and θ is the static contact angle of the liquid phase at the solid surface, which was measured using a goniometer. The contact angle measurement was discussed in the contact angle measurement section of the SI. Deionized (DI) water on the PDMS surface had a contact angle of 96°, as depicted in Figure S2b.

The depth of the channel and throat diameter are depicted as d and $2r$, respectively. Channel depth is fixed, and r is determined by the regular digital disk radius.

The algorithm was designed for circular-shaped solid particles[25] and our model extends its application to solid particles with irregular shapes using the hydraulic diameter of each solid particle. The boundary conditions applied to the model are explained in the boundary and initial conditions section in the SI and are also shown in Figure S4. The pore morphology method is primarily based on the erosion and dilation of the pore spaces using a digital disk. In Figure S3, the algorithm flowchart used for this modeling is depicted. R_{max} and r represent the maximum radius and radius of the digital disk, respectively. The maximum radius was determined to be 50 pixels in this study. At the maximum radius, no void was left using the erosion of pore spaces. We assumed that only lyophobic solid particles can impede the movement of the liquid and lyophilic surfaces can be automatically wetted by liquid upon contact. To apply the erosion process to the interface of the solid and pore, the radius of the digital disk should be modified depending on whether the pixels to be eroded are on a flat or irregular surface.[25,26] The modified radius of the digital disk is shown in eqs 5 and 6.

$$r_1 = r|\cos\theta| \tag{5}$$

$$r_2 = \sqrt{{R_h}^2 + r^2 + 2R_h r\cos\theta} - R_h \tag{6}$$

where r_1 and r_2 represent the modified radius for flat and irregular surfaces, respectively. The regular radius of the digital disk is shown as r, while R_h displays the hydraulic radius of solid particles with an irregular shape. We differentiated the solid particles by employing a MATLAB function, bwlabel. The connectivity check in the algorithm was conducted to make sure that after the erosion process, there was a direct path through the pore spaces to the liquid reservoir, as shown in Figures S4 and S6. After the unconnected pore spaces were removed, the dilation process using the digital disk with a radius of r was performed to return the removed pixels in the erosion process and locate the liquid−gas interface.

To validate the modeling results, we fabricated a microchannel using polydimethylsiloxane (PDMS) based on a scanning electron microscopy (SEM) image of the positive electrode, as shown in Figure S1. The water−air two-phase flow in the transparent microchannel was visualized using an inverted microscope in the experimental setup as shown in Figure 1. We used a pressurizer (OB1MK3+ ELVE FLOW) to control the inlet pressure of the liquid, which was connected to a flow controller. The liquid was then supplied through the reservoir to the inlet of the macroporous channel at the intended pressure. An inverted microscope was utilized for observation. The movement of the interface between the liquid

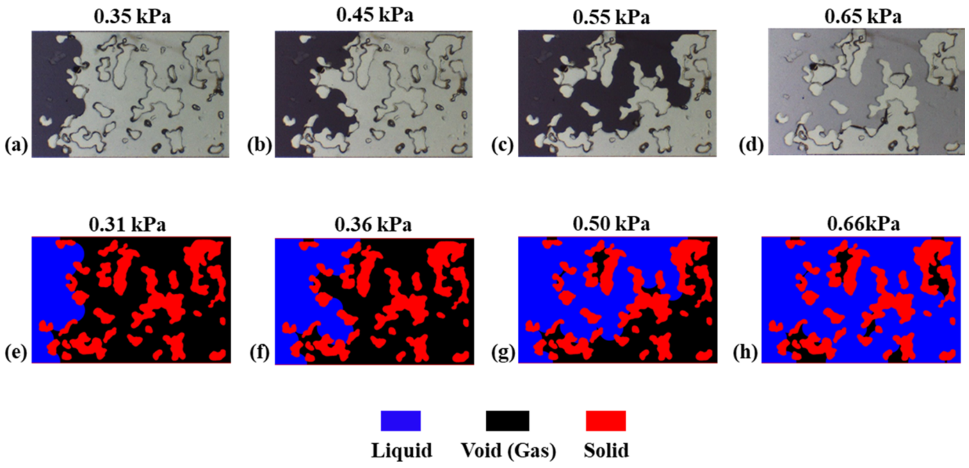

Figure 2. Comparison of the liquid distribution through a porous media achieved from the experiment using fabricated microchannel (a−d) and simulation results (e−h).

and gas phases, water and air, was captured using a 5 megapixel camera connected to the microscope, and the images were transferred to the computer for postprocessing.

The comparison between the experimental results and modeling is shown in Figure 2. We can observe that there is good agreement between the liquid distribution from the experiment and modeling, as depicted in Figure 2a−d and 2e−h, respectively. The discrepancy between the pressure from the experiment and capillary pressure from modeling could be caused by the small differences in the pore structure of the fabricated macroporous channel and the one used in the modeling.

Figure 3 exhibits the comparison of saturation versus capillary pressure of the experiments and modeling. A slight discrepancy in the pressure and saturation levels between the three experiments is observed, which was caused by the sensitivity of the microfluidic devices to the amount of pressure applied to the system. The slight decrease in the experimental saturation level within the pressure range of 0−0.45 mbar was caused by the noise from ambient light, which affected the image processing for counting the pixels. The results showed that this model could simulate the steady state invasion behavior of a nonwetting phase in a macroporous structure with irregular solid particles.

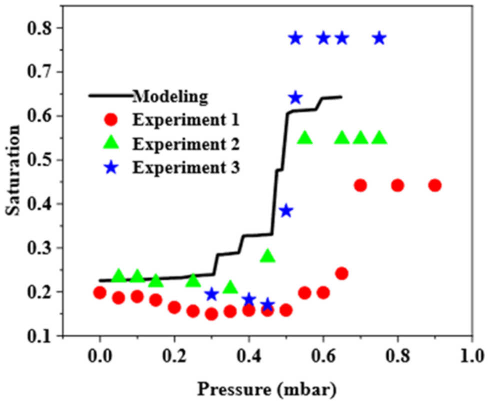

Figure 3. Comparison of capillary pressure versus saturation levels from modeling with the experiments.

To simulate the electrolyte distribution within a porous positive electrode, we implemented the reconstructed porous structure shown in Figure S6. This geometry was reconstructed based on the structure of the microporous layers shown in Figure S1. The reconstruction was done using an efficient digital reconstruction technique that was previously developed in a separate study.[27] The boundary conditions and computational domain are also shown in Figure S6.

2.2. Effective Diffusivity and O_2 Concentration. We calculated the effective diffusivity of the microporous layer and O_2 concentration at each electrolyte saturation using the mass conservation equation, shown in eq 7.

$$\frac{\partial}{\partial x}\left(D_{O_2}\frac{\partial c_{O_2}}{\partial x}\right)+\frac{\partial}{\partial y}\left(D_{O_2}\frac{\partial c_{O_2}}{\partial y}\right)=0 \tag{7}$$

where D_{O_2} and c_{O_2} represent the mass diffusivity and concentration of O_2 in the electrolyte, respectively. We made the local O_2 concentration dimensionless using the oxygen concentration on the left and right boundaries using eq S1. The diffusion coefficient of O_2 in liquid and air was selected as 1.6×10^{-7} and 1.98×10^{-1} cm^2/s, respectively.[28,29] Equation 7 was numerically solved using a simple central differencing scheme from the finite volume method.[30] The boundary conditions and computational domain are listed in Figure S7. The calculated concentration from eq 7 was used to estimate the effective diffusivity of oxygen through the electrode at each electrolyte saturation using eq 8.

$$D_{\mathrm{eff}}=\frac{J_{\mathrm{A}}^{*}W}{C_{\mathrm{R}}-C_{\mathrm{L}}} \tag{8}$$

In which, D_{eff}, J_{A}^{*}, and W show the effective diffusivity, average dimensionless mass flux of O_2, and dimensionless length of the channel. C_{R} and C_{L} represent the dimensionless normalized concentration at the right and left of the computational domain, respectively, shown in Figure S7. We utilized the electrolyte distribution within the microporous layer at each saturation level as a model input. The model was validated using the theoretical/analytical results for a case with a parallel and series arrangement of a solid and liquid (eqs S2 and S3 respectively), which is depicted in Figure S8. The numerical model and results were generated using resources

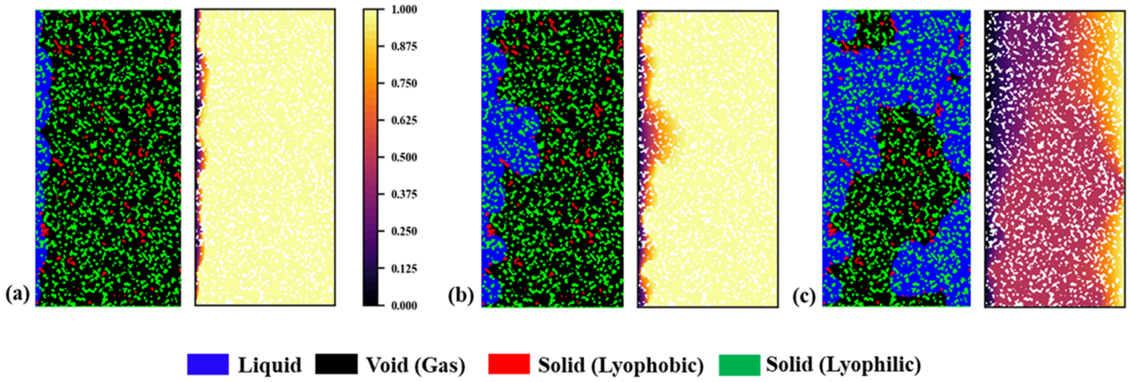

Figure 4. Electrolyte distribution and the corresponding O_2 concentration through the MPL with (a) 6.9%, (b) 18.3%, and (c) 61% saturations. The fractions of PTFE and carbon particles are 10.51 and 89.49%, respectively.

from the ACCESS program.[31] The code used for this analysis along with further documentation is available on GitHub.[1]

3. EXPERIMENTAL DETAILS

This section explains the approach to preparing electrolytes, cell assembly, contact angle measurement, pore volume measurement of the positive electrode, and operating parameters in deep discharge and charge and cycling stability tests.

3.1. Electrolyte Preparation. Tetra ethylene glycol dimethyl ether (TEGDME-99%) was purchased from Sigma-Aldrich and was used to prepare electrolytes in an argon-filled glovebox with H_2O and O_2 of less than 0.01 ppm. Bis(trifluoromethane) sulfonimide lithium salt (LiTFSI) (99.95%) from Sigma-Aldrich was dissolved in TEGDME using a magnetic stirrer for at least 2 h to have a uniform solution with the concentration of 1 mol/L (M).

3.2. Contact Angle. Static contact angles were measured by using a goniometer (rame-hart instrument 250-U4) at room temperature. The contact angle of 1 M LiTFSI in TEGDME, was 104° on the MPL coating, as shown in Figure S2a.

3.3. Preparation of Li–O_2 Cells. The battery consists of negative electrode and positive electrode current collectors, a positive electrode with a diameter of 1.27 cm, a Celgard 2500 separator from Fisher Scientific with a diameter of 1.59 cm, and a lithium chip with a thickness of 0.25 mm and a diameter of 1.56 cm as a negative electrode. A commercially available positive electrode (W1S1011) purchased from the Fuel Cell Store was utilized as the positive electrode. It consisted of a substrate made from carbon cloth coated by mixtures of PTFE binder and Vulcan XC-72R as the microporous layer (MPL) with an average thickness of 100 μm, as shown in Figure S1. The customer-designed current collectors were made from highly corrosion-resistant 316L stainless steel.[32] A parallel channel with height and width of 9 and 9 mm, respectively, and an open ratio of 0.38 was used to supply oxygen to the positive electrode. The separator was soaked in the electrolyte to make sure that it was fully wet before assembly. A specific amount of electrolyte, calculated by the desired saturation, was injected into the MPL and spread over the MPL surface until no excess liquid was left. The negative current collector was separated from the positive current collector by using PTFE gaskets. The thickness of the gaskets was chosen to have a compression ratio of approximately 80% for the internal components. The cell was assembled and tightened appropriately in the glovebox to avoid any leakage before being taken out for electrochemical testing.

3.4. Pore Volume of the Positive Electrode. Ethanol (99%) purchased from Sigma-Aldrich was used to measure the total pore volume of the positive electrode. Ethanol was selected for its low surface tension $22.85 \times 10^{3}\frac{N}{m}$[33] and high capability to wet the positive electrode. By measuring the weight difference between the dry electrode and the electrode fully saturated by ethanol with a density of 0.789 g/mL, the total pore volume of the positive electrode with a diameter of 1.27 cm was calculated as 44.9 ± 1.28 μL. It should be mentioned that this was the pore volume of the MPL and carbon cloth substrate together. The total pore volume of the positive electrode was used to determine the saturation level of the electrolyte. We applied 44.9, 27, 18, and 9 μL of the TEGDME electrolyte, corresponding to the saturation levels of 100, 60, 40, and 20%, respectively.

3.5. Double-Layer Capacitance. The electrochemically active surface area of the positive electrode at different saturations was estimated by using double-layer capacitance (DLC) by cyclic voltammetry (CV). The CV tests were conducted using a Squidstat Prime potentiostat from Admiral Instruments inside the glovebox. The DLC of symmetric cells made from two positive electrodes at controlled saturation levels sandwiched a Celgard separator. CV tests were conducted at ±0.1 V around the open circuit voltage (OCV) at scanning rates ranging from 0.3 to 20 mV/s. The DLC is calculated using eq 9.[34]

$$C_{\text{total}} = \frac{1}{2\nu(\eta_a - \eta_c)} \int_{\eta_c}^{\eta_a} i(\eta)\mathrm{d}\eta \tag{9}$$

In which, ν, η_a, and η_c are scan rate, the maximum polarization in the negative electrode and positive electrode direction, respectively. The current density as a function of the voltage is shown as $i(\eta)$. C_{total} represents the total capacitance, mF/cm^2, including the DLC and pseudo capacitance. The total capacitance values achieved from eq 9 are plotted versus $\frac{1}{\sqrt{\nu}}$, and the Y-axis intercept of the linear-curve fitting of the data points shows the DLC.[35]

3.6. Ohmic Resistance. The ohmic resistance of the separator and the positive electrode was determined by using the electrochemical impedance spectroscopy (EIS) method. We first measured the ohmic resistance of the separator using the symmetric cell made from two lithium chips sandwiching a Celgard separator.[34] The galvanostatic mode with starting and ending frequencies of 1 MHz and 0.1 Hz was applied. The DC bias current and AC excitation amplitude were set to 0 A and 20 μA, respectively. Similarly, the symmetric cells made from two positive electrodes, with controlled electrolyte saturation, sandwiching a Celgard separator, were used to measure the total ohmic resistance. The frequency range applied to the cell using galvanostatic mode was from 5 kHz to 0.1 Hz with the DC bias current and AC excitation amplitude of 0 A and 20 μA, respectively.

3.7. Deep Discharge and Charge Capacities and Cycling Test. Assembled battery cells were connected to a four-channel battery tester, a Squidstat Prime from Admiral Instruments. Pure oxygen was supplied at a flow rate of 3 standard cubic centimeters per minute, SCCM, for each battery cell. All cells were assembled in the glovebox before taking out and purged with pure oxygen for 3 h under OCV at room temperature. All tests were performed at a current density of 0.1 mA/cm^2 for both the discharge and charge processes. The discharge and charge cutoff voltage were set to 2 and 4.5 V, respectively. For cycling stability, the cutoff areal capacity was set to 0.5 mAh/cm^2.

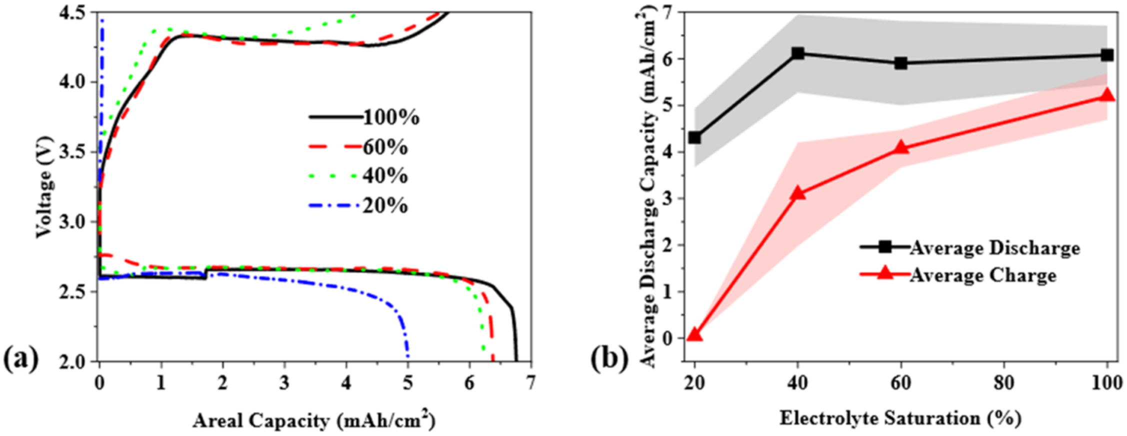

Figure 5. Comparison of (a) maximum areal discharge−charge capacity at different saturation levels and (b) average of the three capacities at each saturation level.

4. RESULTS AND DISCUSSION

First, we used our model, explained in Section 2, to simulate the electrolyte distribution through the porous positive electrode. This visualization gave us an understanding of the heterogeneity of the electrolyte distribution at different saturation levels, affecting the oxygen concentration and wetting behavior of the positive electrode. Second, we investigated the saturation effect on the deep discharge and charge capacities and cycling performance. Furthermore, the impact of the wettability of positive electrodes on electrolyte saturation and ionic conductivity was studied. It should be noted that the saturation levels in the experiment were calculated according to the supplied volume of the electrolyte, resulting in 100, 80, 60, 40, and 20%. However, the saturation level in the modeling was determined by the capillary pressure. Therefore, we aimed to match the closest electrolyte saturations between experiments and modeling.

4.1. Electrolyte Distribution in the Porous Positive Electrode.

Figure 4 displays the electrolyte distribution with the corresponding dimensionless concentration of the O_2 through the reconstructed porous geometry at three different saturation levels. The height and width of the porous geometry are 108 and 54 μm, respectively, which is depicted in Figure S6. Red solid particles are representative of PTFE particles with a volume fraction of 10.51% and a contact angle of 105°, while green solid particles show the carbon particles, considered lyophilic with the fraction of 89.49%. The liquid phase (electrolyte) and gas phase (air) are depicted in blue and black, respectively. It was assumed that the flow was capillary-dominated and viscous forces were neglected. Figure 4a depicts the electrolyte distribution at a saturation of 6.9% and the average dimensionless O_2 concentration of 0.7 at the wetted surface. It showed that the electrolyte interface reached lyophilic areas (carbon particles) as long as it was not impeded by lyophobic particles (PTFE). In Figure 4b, more electrolytes were supplied, corresponding to a saturation of 18.3% and an O_2 concentration of 0.69. Although more solid surfaces were wetted, the average O_2 concentration at the wetted surface remained almost unchanged. This was attributed to the fast diffusion of the O_2 in the gas phase and the relatively short O_2 diffusion path in the liquid at this saturation level. The O_2 concentration at the wetted surface showed a significant decrease to 0.37 at the saturation of 61.2%, as depicted in Figure 4c. It resulted from the filled pore spaces with the electrolyte, particularly at the right boundary, where the O_2 entered the positive electrode. The gas-trapped regions, shown in Figure 4c, could act as highways for the diffusion of the O_2 to reach the wetted surface.

4.2. Deep Discharge and Charge.

The discharge and charge curves with the highest capacity at the four electrolyte saturations are displayed in Figure 5a. The highest areal discharge capacity of 6.76 mAh/cm^2 was obtained at 100% saturation. When the saturation decreased to 60 and 40%, there were only a 5.6 and 7.7% reduction (6.38 and 6.24 mAh/cm^2) in discharge capacity. A considerable decrease in discharge capacity (5.03 mAh/cm^2) was observed at a saturation of 20%. This significant reduction in capacity could be attributed to the insufficient electrolyte to get the positive electrode surface wet. As we observed in Figure 4b, the positive electrode with 18.3% saturation showed a relatively high average O_2 concentration (0.69) at the wetted surface, but these wetted regions were not enough for ORR. On the other hand, the positive electrode with 61.2% saturation, as shown in Figure 4c, had a lower O_2 concentration (0.37) at the wetted surface but more wetted surface areas for ORR, which compensated for the lower average O_2 concentration.

The deep charge capacity at 60% saturation was only 2.3% lower than that at 100% positive electrode saturation, 5.52 and 5.65 mAh/cm^2, respectively. When the saturation decreased to 40%, a 22.65% reduction in the charge capacity was observed. A negligible charge capacity of 0.042 mAh/cm^2 was achieved at 20% saturation. This was mostly attributed to the dry positive electrode surface areas, resulting in the sudden increase of charging voltage and reaching cutoff voltage, which was also observed by Matsuda et al.[20] In Figure 5b, a summary of the average discharge and charge capacity is shown. By decreasing the electrolyte saturation from 100 to 40%, the average discharge capacity remained almost the same (0.6% increase). In comparison, the average charge capacity decreased by 40.46%. These results showed that by decreasing the electrolyte saturation to 60%, no considerable degradation in discharge and charge capacity was observed. This helps us to decrease the internal weight of the battery with a negligible change in capacity.

Energy density is a crucial factor in determining achievable energy, calculated using the weight of all of the internal components. Table 1 displays the energy density and charging efficiency at the four saturation levels. The weight of

Table 1. Comparison of Discharge Energy Density at Each Saturation Level Based on the Average of the Maximum Discharge Capacity and Charging Efficiency at Each Saturation

saturation level (%)	energy density (Wh/kg)	charging efficiency (%)
100	172.91	85.36
60	247.13	57.98
40	238.54	50.53
20	187.85	1.25

electrolytes at 100, 60, 40, and 20% saturations was measured at 53, 31, 21, and 10 mg, respectively. The mass of the dry positive electrode, fully wet Celgard 2500 separator, and lithium chip were recorded as 29, 12, and 23 mg, respectively. It should be noted that the energy density was measured according to the average discharge capacity and average discharge voltage at each saturation level. It was shown that the highest energy density corresponded to 60% saturation with 247.13 Wh/kg, while it was 238.55 Wh/kg for a 40% saturation level. Increasing the electrolyte amount to 100% decreased the energy density to 172.91 Wh/kg, which was even lower than that with the 20% saturation (187.85 Wh/kg). Furthermore, the battery with 100% saturation achieved a charging efficiency of 85.36%, while those with 60 and 40% could get charging efficiency of 57.98 and 50.53%, respectively. The minimum charging efficiency was achieved at 20% saturation due to the negligible charging capacity, as discussed earlier. It was revealed that while the battery with 100% saturation could get higher charging efficiency, partially wet positive electrodes, 40 and 60%, have higher energy densities.

4.3. Cycling Stability.

In this section, we investigated the impact of electrolyte saturation on the cycling stability of Li−O_2 batteries. All cycling tests were performed at a current density of 0.1 mA/cm^2 for both discharge and charge processes with the limited areal capacity of 0.5 mAh/cm^2, as shown in Figure 6. Figure 6a displays the cycling performance at 100% saturation. It completed 10 cycles before the discharge voltage reached cutoff. Similarly, the battery with 60% saturation could achieve nine cycles, while the one with 40% saturation could complete 14 cycles. The battery with the least electrolyte amount, 20% saturation, had the lowest cyclability with only three cycles. In the third cycle, the overpotential sharply increased, and the charge cutoff voltage was reached. This could be attributed to the electrolyte shortage and electrolyte movement toward the gas diffusion layer because of lithium peroxide formation. Although the solid discharge products start to decompose during the OER process, the bulk electrolyte may not be able to fully return to the porous positive electrode near the separator, which can create a dry region in the positive electrode without any path for the ions to transfer. It should be noted that the number of cycles discussed here was according to the criterion of discharge voltage cutoff point. Since it could not show the efficiency of cycling at each

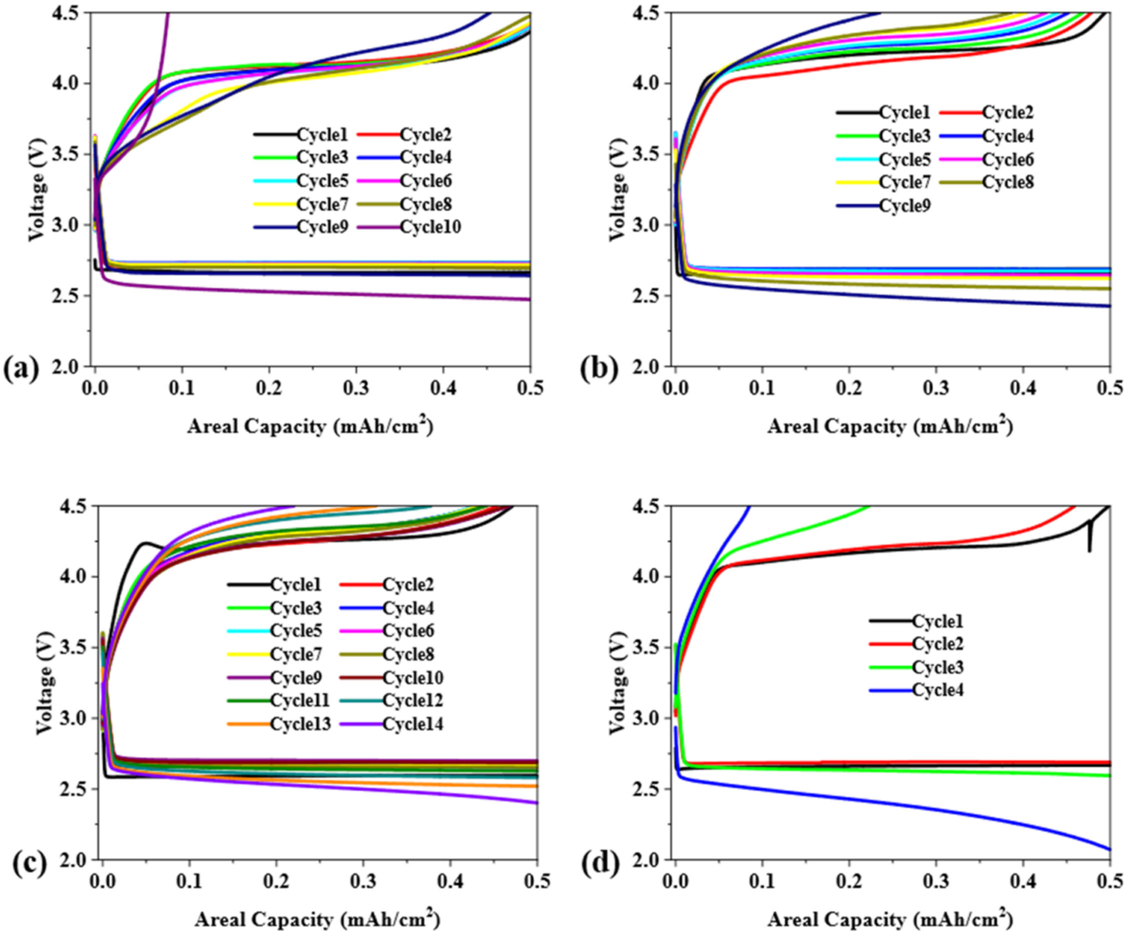

Figure 6. Discharge−charge cycles at a limited areal capacity of 0.5 mAh/cm^2 and discharge−charge current density of 0.1 A/cm^2 at (a) 100% saturation, (b) 60% saturation, (c) 40% saturation, and (d) 20% saturation.

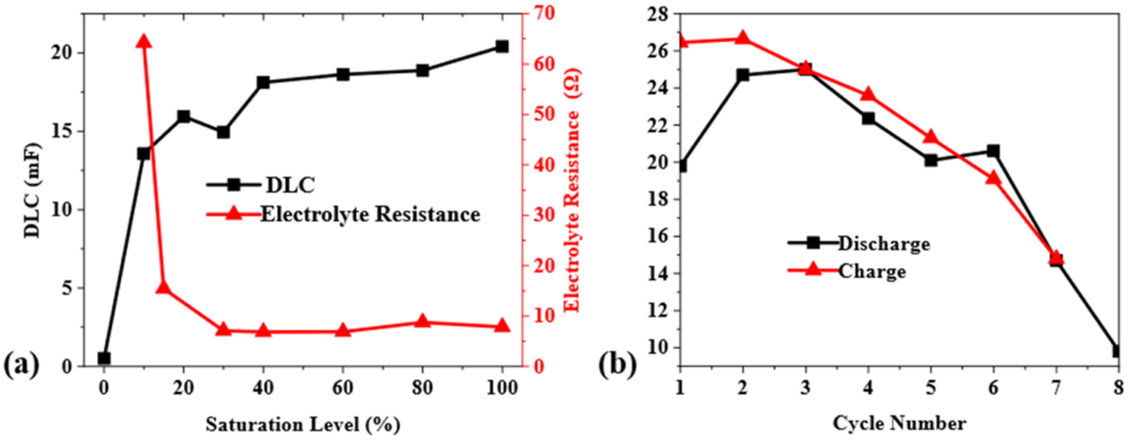

Figure 7. Double-layer capacitance and ohmic resistance of (a) a symmetric positive electrode cell at different electrolyte saturation levels and (b) the battery cell with 100% initial saturation level during cycling with the limited capacity of 1 mAh/cm^2.

saturation, the cycling efficiency is discussed in the following section.

To better understand the effect of the saturation level on cycling performance, we measured the charging efficiency and overpotential during cycling, as shown in Table S1. It was shown that the charging efficiency decreased during cycling for both fully and partially wet positive electrodes. The battery cycled with the average efficiency of 98.86% for nine cycles at 100% saturation. It dropped sharply to 16.73% in cycle 10th. On the other hand, the battery with partial wetting, 40% saturation, cycled with an average efficiency of 89.09% for 11 cycles. The efficiency started to decrease considerably from cycle 12th until it reached 44.02% at cycle 14th. The battery with 60% saturation showed an average efficiency of 88.76% up to cycle eighth. However, the efficiency dropped to 47.02% at cycle ninth. For the first five cycles, the battery with 60% saturation performed with a higher charging efficiency compared to 40% saturation. However, from cycle six forward, the battery with 40% saturation showed a charging efficiency higher than that with 60% saturation. Indeed, the battery cycled 11 and eight times before a significant reduction in charging efficiency at 40 and 60% saturation, respectively. The battery with the least amount of electrolyte, 20% saturation, experienced a sharp reduction in charging efficiency only after two cycles, reaching 44.52% in the third cycle. Furthermore, the battery with the fully wet positive electrode showed an overpotential in the range of 1.26−1.39 V and an average of 1.33 V. In comparison, partially wet positive electrodes, 40 and 60% showed an overpotential range of 1.48−1.69 and 1.43−1.71 V with an average of 1.58 and 1.56 V, respectively. The lower overpotential of fully wet electrodes compared to partially wet electrodes can be ascribed to two factors. First, at low current density (0.1 mA/cm^2), there is less demand for O_2 compared to high current density, resulting in better performance (lower overpotential) in fully wet electrodes than partially wet ones due to higher wetted areas.[14] Second, the electrolyte distribution at saturation (<100%) gets more heterogeneous, leading to a decrease in effective electrochemical surface and an increase in overpotential.[20] It was depicted that the significant increase in the charge voltage and decrease in discharge voltage took place earlier, in cycle 10th, at 100% saturation compared to 40% saturation, which occurred in cycle 14th. This could be attributed to two factors. First, it becomes more difficult for O_2 to diffuse through pore spaces filled with the electrolyte due to the lower O_2 diffusivity in liquids, resulting in lower oxygen concentration in wetted surface, which was also reported by Matsuda et al.[20] Second, the discharge products formed during cycling are likely to push out the electrolyte toward the oxygen channel, which can clog the O_2 diffusion paths and consequently decrease the O_2 concentration.[36,37] In this condition, when the positive electrode is partially wet, not all of the O_2 diffusion paths are filled with liquid electrolyte and some paths filled with gas remain, paving the way for O_2 diffusion. To quantitatively correlate the battery capacity and cycling stability with the internal wettability of the partially and fully wet positive electrodes, the electrochemically active surface area, effective diffusivity, and electrolyte resistance were measured and exhibited in the following sections.

4.4. Electrochemically Active Surface Area and Ohmic Resistance.

The electrochemically active surface area gives us an understanding of the internal wettability of the fully and partially wet positive electrodes. Figure 7a exhibits the change in DLC at different electrolyte saturations. The DLC increased significantly from 0.51 to 13.55 mF by increasing the saturation level from 0 to 10%. The DLC showed a moderate increase to 18.11 mF at 40% saturation, and it gradually increased to 20.4 mF at 100% saturation. It is worth mentioning that in the experiment, the coating layer, MPL, was attached to the carbon cloth as the gas diffusion layer, which was lyophilic for the electrolyte. Consequently, by injecting more electrolyte volume, the excess electrolyte moved to the gas diffusion layer. As a result, the DLC did not increase significantly after saturation reached 40% or higher. Meanwhile, the liquid likely forms a thin film over the solid surface once the electrolyte is in contact with the carbon surface due to the lipophilicity, and the wetted solid surface contributes to the DLC. This phenomenon results in a high DLC at the electrolyte saturation of 40%. The above results can also explain that the low discharge capacity, 3.99 mAh/cm^2, and low cycling stability, three cycles, at 20% saturation, were likely caused by insufficient wetted surface areas. Moreover, the behavior of DLC depicted that for the positive electrode used in this study, 40% electrolyte saturation was sufficient to provide reaction sites for the ORR.

An important parameter showing the ionic conductivity within a positive electrode is the ohmic resistance. Figure S10 depicts the high-frequency impedance spectrum of a singlelayer Celgard 2500 separator. The *x*-axis intercept of the linear-fit curve, which is 7.53 Ω, represents the ohmic resistance of the separator. Figure S11 displays the impedance spectrum values of the positive electrode at different electrolyte saturation. It was shown that for each saturation, there were two slopes corresponding to the high and low-frequency regions with the frequency range of 5 kHz to 2 and 2−0.1 Hz, respectively.[34,38] Figure 7a exhibits the relationship between the electrolyte saturation and the ohmic resistance of the positive electrode. There was a significant decrease in electrolyte resistance by increasing the saturation from 10 to 30%, corresponding to 64.22 and 7.08 Ω, respectively. It was shown that the ohmic resistance did not change considerably for saturation levels greater than 30%. Indeed, the ohmic resistance of the electrode depends on the electrolyte distribution or tortuosity of the porous structure. If there is a shorter path for the ions to transfer through the electrolyte, the ohmic resistance of the electrode is smaller. The above results revealed that the battery with a saturation of less than 30% could suffer from a low ionic conductivity. For instance, the battery with 20% saturation showed a low charge capacity (0.04 mAh/cm^2) and poor cycling performance (three cycles). Once the saturation is greater than 30%, the ionic conductivity of electrodes was not the limiting factor.

As we discussed the impact of electrolyte saturation on the internal wetting behavior of the symmetric positive electrode, we investigated how the internal wettability of a positive electrode changed during cycling under a limited discharge/charge capacity of 1 mAh/cm^2. The CV test was performed at ±0.1 V around the OCV using different scan rates to quantify the DLC. Figure 7b demonstrates the DLC values determined after each discharge and charge cycle. It shows a downward trend for both discharge and charge cycling except for the second discharge cycle, which increased from 19.8 to 24.7 mF. It could be ascribed to the movement of the electrolyte within the positive electrode due to the deposition and decomposition of the solid discharge product.[39] The DLC gradually reduced from 24.7 mF at the second discharge cycle to 20.6 mF at the sixth cycle. It started to drop significantly, reaching 9.8 mF in the eighth cycle. The moderate decrease in DLC could be attributed to the deposition of lithium peroxide solid particles over the positive electrode surface. Since discharge products have poor electrical conductivity, the formation of discharge products on the electrode surface leads to the reduction of DLC. The sharp decrease after the sixth discharge cycle could be caused by the decomposition of the positive electrode structure and also the formation of solid lithium−carbonate-based side products due to the decomposition of the electrolyte solvent during cycling. It has been shown that side products, such as lithium carbonate, can form during repeated cycling, which is difficult to decompose during the charging process.[20,23] In the charging process, there was no considerable change in DLC for the first two cycles, while it started to decrease after the second cycle. The DLC decreased during charge cycling from 26.45 to 14.8 mF from the first cycle to the seventh cycle. The comparison of the DLC values after discharge and charge for the same cycle showed that it increased gradually after the charging process, resulting from the decomposition of solid discharge products. However, for the fifth and sixth cycles, the DLC values were slightly less than the corresponding discharge values. This could be attributed to the production of lithium−carbonate-based products as a result of side reactions. Moreover, it could be caused by the decomposition of the positive electrode structure, leading to the reduction of reaction sites and consequently smaller wetted surface areas contributing to DLC. These results supported our reasoning for the decrease and increase in discharge and charge voltage during cycling, shown in Figure 6.

4.5. Effective Diffusivity.

It is helpful to understand how effective diffusivity and the O_2 concentration within the positive electrode change with the electrolyte saturation. Both effective diffusivity and O_2 concentration were nondimensionalized and normalized, as discussed in Section 2.2 and eq S1, in the SI to have a reasonable comparison. Figure 8 compares the effective diffusivity of the microporous layer with the average dimensionless concentration of the O_2 at the boundary of the wetted surfaces of the positive electrode at different electrolyte saturations. It is shown that by increasing the saturation to around 18%, the effective diffusivity decreased significantly from 1 to 0.55. In contrast, the average concentration of the O_2 at the wetted surfaces remained almost constant at around 0.7. This is attributed to the thin layer of bulk electrolyte within the MPL, providing short O_2 diffusion paths, as shown in Figure 4a. We could observe a considerable reduction in both effective diffusivity and the concentration of the O_2, reaching 0.17 and 0.37, respectively, at 60% saturation. This is ascribed to the increase in bulk electrolyte filling the pore spaces, resulting in a longer diffusion path for O_2 in the liquid phase, as shown in Figure 4c. By increasing the saturation to 100%, the effective diffusivity decreased to 0.042, while the average O_2 concentration remained almost constant around 0.37. Indeed, the O_2 concentration at the wetted surface of the carbon particles close to the right boundary (gas diffusion layer) is higher than those close to the separator, resulting in an insignificant change in the average O_2 concentration for saturation greater than 60%. These results showed that by decreasing the electrolyte saturation to 60%, there was no significant increase in the average O_2 concentration in the wetted surface areas, while a considerable increase was observed for saturation less than 60% (e.g., 40%). This could explain the higher cycling performance at 40% with 14 cycles compared to 60 and 100% saturation with nine and 10 cycles, respectively, before the discharge voltage reached cutoff. Indeed, the higher average O_2 concentration at the boundary of the electrode-wetted surfaces of 40% compared to 60 and

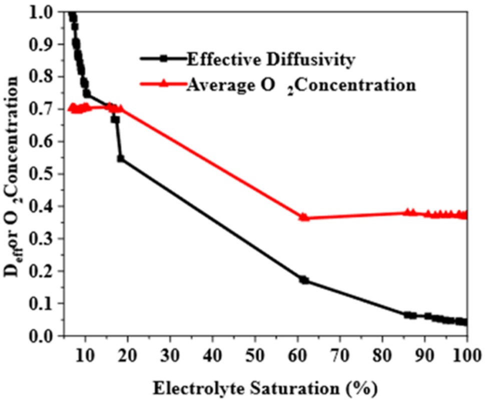

Figure 8. Comparison of the normalized dimensionless effective diffusivity of the positive electrode microporous layer with normalized dimensionless average O_2 concentration at wetted surfaces of the positive electrode at different electrolyte saturations.

100% saturation caused the battery with 40% failure later than 60 and 100% saturation.

4.6. Effect of Electrolyte Evaporation. We investigated the maximum possible electrolyte evaporation rate to analyze how much electrolyte loss due to evaporation could affect the positive electrode wetting behavior. It was assumed that the partial pressure of the electrolyte was the same as the saturation pressure at the outlet of the cell, explained in the maximum electrolyte evaporation rate section in the SI and eq S4. Table S2 depicts the following observations: (1) electrolyte loss due to the evaporation at each saturation, (2) the corresponding change in DLC, and (3) effective diffusivity, which were quantified using the nonlinear curve fitting, shown in Figure S9. It should be noted that this electrolyte loss was calculated according to the initial electrolyte volume at each saturation and the corresponding experiment time. The minimum and maximum electrolyte loss (6.14 and 13.93%) were measured at 100 and 20% electrolyte saturation, respectively. According to the electrolyte loss, the change in DLC was insignificant for saturation of 100, 60, and 40% (less than 1.15%), while it reduced by 4.63% at the initial saturation of 20%. The effective diffusivity increased by 37.61% at the initial saturation of 100%, while the increase was lower for initial saturation of 60, 40, and 20%, corresponding to 20.17, 16.58, and 8.28%, respectively. The reason for the significant increase in effective diffusivity at 100% saturation was the formation of some pore spaces occupied by gas, making the O_2 diffusion easier. This analysis revealed that evaporation could be a double-edged sword in positive electrode wettability. On one hand, it resulted in the reduction of wetted areas of the positive electrode. On the other hand, it could improve the effective diffusivity, particularly for the fully saturated positive electrode.

5. CONCLUSIONS

In conclusion, our study highlights the influence of electrolyte saturation and distribution on deep discharge and charge capacities and cycling stability of Li−O_2 batteries. We investigated the internal wettability of the positive electrodes, electrolyte distribution, and the O_2 concentration at the wetted surfaces at different electrolyte saturations using models and experiments.

- We found that by decreasing the electrolyte saturation to 40%, the average discharge capacity was almost the same as the fully wet cathode, 6.1 and 6.08 mAh/cm^2, respectively. However, the average charge capacity, 40% saturation, achieved a lower charge capacity (3.09 mAh/cm^2) than the electrode with 100% saturation (5.19 mAh/cm^2). This could be attributed to electrolyte movement due to discharge product deposition, resulting in more heterogeneous electrolyte distribution at 40% compared to 100% saturation.
- The highest energy density was achieved at 247.13 Wh/kg for 60% electrolyte saturation, showing the optimum electrolyte amount regarding the battery's internal component weight and discharge capacity.
- The highest number of cycles (before reaching discharge cutoff voltage) was achieved for the battery with 40% saturation; however, the fully wet battery showed a higher average charging efficiency (98.96%) compared to the 40% saturation (89.09%). This was ascribed to the lower demand for the O_2 at low current density (0.1 mA/cm^2), and more uniform electrolyte distribution at 100% saturation, which resulted in a lower overpotential for the fully wet battery.
- We depicted that the minimum electrolyte saturation of 40% was sufficient to provide enough reaction sites (wetted surface areas) within the positive electrode. Similarly, 30% saturation could provide a low ohmic resistance (7.08 Ω) compared to the fully wet electrode with (∼7 Ω).
- The average O_2 concentration at the boundary of the wetted surfaces was considerably higher at 40% compared with 60 and 100% saturation.

These findings contribute to a deeper understanding of the effect of electrolyte saturation, porous structures of electrodes, and internal wettability on the Li−O_2 performance to obtain high capacity and energy density. Although our model has limitations, it could depict the electrolyte distribution within a porous electrode according to the contact angle of the electrolyte on the electrode, which is extremely difficult to observe experimentally due to the small scale (nanometers) of the porous electrodes. A comprehensive understanding of the influence of porous structure on the mass transfer within the positive electrodes facilitates the future development of positive electrodes. Based on this study, the design of positive electrodes with gradient porosity and controlled wettability could be a promising research direction.

■ ASSOCIATED CONTENT

Supporting Information

The Supporting Information is available free of charge at https://pubs.acs.org/doi/10.1021/acsami.4c12168.

> The microporous geometry utilized for pore structure reconstruction, flowchart of the implemented pore morphology algorithm, contact angle measurement, boundary conditions considered in the modeling, EDX analysis of the microporous layer, validation of the model used for effective diffusivity and O_2 concentration, maximum possible electrolyte evaporation rate at different saturation, and ionic conductivity using the EIS method along with the impedance spectrum data analysis (PDF)

■ AUTHOR INFORMATION

Corresponding Author

Xianglin Li − *Department of Mechanical Engineering and Materials Science, Washington University in St Louis, St Louis, Missouri 63130, United States; Department of Mechanical Engineering, University of Kansas, Lawrence, Kansas 66045, United States;* orcid.org/0000-0002-0193-9410; Phone: +1 (314) 935-3249; Email: lxianglin@wustl.edu

Authors

Amirhossein Sarabandi − *Department of Mechanical Engineering and Materials Science, Washington University in St Louis, St Louis, Missouri 63130, United States*

Andre Adam − *Department of Mechanical Engineering, University of Kansas, Lawrence, Kansas 66045, United States*

Complete contact information is available at: https://pubs.acs.org/10.1021/acsami.4c12168

Notes

The authors declare no competing financial interest.

■ ACKNOWLEDGMENTS

The authors highly appreciate the support from the National Science Foundation (Award 1941083 and 2329821). This work used Expanse (GPU) at SDSC through allocations MAT210014 and MAT230071 from the Advanced Cyberinfrastructure Coordination Ecosystem: Services & Support (ACCESS) program, which is supported by the National Science Foundation under grants #2138259, #2138286, #2138307, #2137603, and #2138296. Additional instrument support is provided by the Institute of Materials Science and Engineering (IMSE) at Washington University in St. Louis.

■ ADDITIONAL NOTE

[1] GitHub: https://github.com/adama-wzr/EffectiveDiffusivityFVM.

■ REFERENCES

(1) Liu, T.; Vivek, J. P.; Zhao, E. W.; Lei, J.; Garcia-Araez, N.; Grey, C. P. Current Challenges and Routes Forward for Nonaqueous Lithium−Air Batteries. *Chem. Rev.* **2020**, *120* (14), 6558−6625.

(2) Kwak, W.-J.; Rosy; Sharon, D.; Xia, C.; Kim, H.; Johnson, L. R.; Bruce, P. G.; Nazar, L. F.; Sun, Y.-K.; Frimer, A. A.; Noked, M.; Freunberger, S. A.; Aurbach, D. Lithium−Oxygen Batteries and Related Systems: Potential, Status, and Future. *Chem. Rev.* **2020**, *120* (14), 6626−6683.

(3) Wang, F.; Li, X. Effects of the Electrode Wettability on the Deep Discharge Capacity of Li−O_2 Batteries. *ACS Omega* **2018**, *3* (6), 6006−6012.

(4) Lu, Y.-C.; Gasteiger, H. A.; Parent, M. C.; Chiloyan, V.; Shao-Horn, Y. The Influence of Catalysts on Discharge and Charge Voltages of Rechargeable Li−Oxygen Batteries. *Electrochem. Solid-State Lett.* **2010**, *13* (6), A69.

(5) Li, Y.; Wang, X.; Dong, S.; Chen, X.; Cui, G. Recent Advances in Non-Aqueous Electrolyte for Rechargeable Li−O_2 Batteries. *Adv. Energy Mater.* **2016**, *6* (18), No. 1600751.

(6) Olivares-Marín, M.; Palomino, P.; Enciso, E.; Tonti, D. Simple Method to Relate Experimental Pore Size Distribution and Discharge Capacity in Cathodes for Li/O_2 Batteries. 2014. DOI: 10.13039/501100003329.

(7) Yu, Z.; Carter, R. N.; Zhang, J. Measurements of Pore Size Distribution, Porosity, Effective Oxygen Diffusivity, and Tortuosity of PEM Fuel Cell Electrodes. *Fuel Cells* **2012**, *12* (4), 557−565.

(8) Wang, F.; Li, X. Discharge Li-O_2 Batteries With Intermittent Current. *J. Power Sources* **2018**, *394*, 50−56.

(9) Xia, C.; Bender, C. L.; Bergner, B.; Peppler, K.; Janek, J. An Electrolyte Partially-Wetted Cathode Improving Oxygen Diffusion in Cathodes of Non-Aqueous Li−Air Batteries. *Electrochem. Commun.* **2013**, *26*, 93−96.

(10) Xu, W.; Xiao, J.; Wang, D.; Zhang, J.; Zhang, J.-G. Effects of Nonaqueous Electrolytes on the Performance of Lithium/Air Batteries. *J. Electrochem. Soc.* **2010**, *157* (2), A219.

(11) Li, Q.; Zhang, T.; Zhang, T.; Xue, Z.; Sun, H. Study on Two-Phase Permeation of Oxygen and Electrolyte in Lithium Air Battery Electrode Based on Digital Twin. *Energies* **2022**, *15* (19), 6986.

(12) Wang, Y.; Hao, L. Effects of Cathode Structure on the Discharge Performance of Non-Aqueous Li-O_2 Batteries. *Electrochim. Acta* **2022**, *425*, No. 140703.

(13) Wang, F.; Li, X. Pore-Scale Simulations of Porous Electrodes of Li−O_2 Batteries at Different Saturation Levels. *ACS Appl. Mater. Interfaces* **2018**, *10* (31), 26222−26232.

(14) Mayur, M.; Bessler, W. G. Two-Dimensional Computational Fluid Dynamics Analysis of Transport Limitations of Different Electrolyte Systems in a Lithium-Air Button Cell Cathode. *J. Electrochem. Soc.* **2017**, *164* (11), E3489−E3498.

(15) Gwak, G.; Ju, H. Three-Dimensional Transient Modeling of a Non-Aqueous Electrolyte Lithium-Air Battery. *Electrochim. Acta* **2016**, *201*, 395−409.

(16) Xiao, J.; Wang, D.; Xu, W.; Wang, D.; Williford, R. E.; Liu, J.; Zhang, J.-G. Optimization of Air Electrode for Li/Air Batteries. *J. Electrochem. Soc.* **2010**, *157* (4), A487.

(17) Saengkaew, J.; Kameda, T.; Ono, M.; Matsuda, S. Self-Standing Porous Carbon Electrodes for Lithium−Oxygen Batteries Under Lean Electrolyte and High Areal Capacity Conditions. *Mater. Adv.* **2022**, *3* (8), 3536−3544.

(18) Blunt, M. J. *Multiphase Flow in Permeable Media: A Pore-Scale Perspective*; Cambridge University Press: Cambridge, 2017.

(19) Matsuda, S.; Ono, M.; Yamaguchi, S.; Uosaki, K. Criteria for Evaluating Lithium−Air Batteries in Academia to Correctly Predict Their Practical Performance in Industry. *Mater. Horiz.* **2022**, *9* (3), 856−863.

(20) Matsuda, S.; Yamaguchi, S.; Yasukawa, E.; Asahina, H.; Kakuta, H.; Otani, H.; Kimura, S.; Kameda, T.; Takayanagi, Y.; Tajika, A.; Kubo, Y.; Uosaki, K. Effect of Electrolyte Filling Technology on the Performance of Porous Carbon Electrode-Based Lithium-Oxygen Batteries. *ACS Appl. Energy Mater.* **2021**, *4* (3), 2563−2569.

(21) Ono, M.; Saengkaew, J.; Matsuda, S. Poor Cycling Performance of Rechargeable Lithium−Oxygen Batteries under Lean-Electrolyte and High-Areal-Capacity Conditions: Role of Carbon Electrode Decomposition. *Adv. Sci.* **2023**, *10* (24), No. 2300896.

(22) Lee, H.; Lee, D. J.; Kim, M.; Kim, H.; Cho, Y. S.; Kwon, H. J.; Lee, H. C.; Park, C. R.; Im, D. High-Energy Density Li−O_2 Battery With a Polymer Electrolyte-Coated CNT Electrode via the Layer-by-Layer Method. *ACS Appl. Mater. Interfaces* **2020**, *12* (15), 17385−17395.

(23) Matsuda, S.; Yasukawa, E.; Kameda, T.; Kimura, S.; Yamaguchi, S.; Kubo, Y.; Uosaki, K. Carbon-Black-Based Self-Standing Porous Electrode for 500 Wh/kg Rechargeable Lithium-Oxygen Batteries. *Cell Rep. Phys. Sci.* **2021**, *2* (7), No. 100506.

(24) Matsuda, S. Rechargeable Lithium-Air Batteries With Practically High Energy Density. *Electrochemistry* **2023**, *91* (10), 101006.

(25) Liu, X.; Zhou, A.; Shen, S.; Li, J. Modeling Drainage in Porous Media Considering Locally Variable Contact Angle Based on Pore Morphology Method. *J. Hydrol.* **2022**, *612*, No. 128157.

(26) Schulz, V. P.; Wargo, E. A.; Kumbur, E. C. Pore-Morphology-Based Simulation of Drainage in Porous Media Featuring a Locally Variable Contact Angle. *Transp. Porous Med.* **2015**, *107* (1), 13−25.

(27) Adam, A.; Wang, F.; Li, X. Efficient Reconstruction and Validation of Heterogeneous Microstructures for Energy Applications. *Int. J. Energy Res.* **2022**, *46* (15), 22757−22771.

(28) Gittleson, F. S.; Jones, R. E.; Ward, D. K.; Foster, M. E. Oxygen Solubility and Transport in Li−Air Battery Electrolytes: Establishing Criteria and Strategies for Electrolyte Design. *Energy Environ. Sci.* **2017**, *10* (5), 1167−1179.

(29) Schmitz, D.; Anlauf, R.; Rehrmann, P. Effect of Air Content on the Oxygen Diffusion Coefficient of Growing Media. *AJPS* **2013**, *04* (05), 955−963.

(30) Adam, A.; Fang, H.; Li, X. Effective Thermal Conductivity Estimation Using a Convolutional Neural Network and Its Application in Topology Optimization. *Energy AI* **2024**, *15*, No. 100310.

(31) Boerner, T. J.; Deems, S.; Furlani, T. R.; Knuth, S. L.; Towns, J. ACCESS: Advancing Innovation: NSF's Advanced Cyberinfrastructure Coordination Ecosystem: Services & Support. In *Practice and Experience in Advanced Research Computing*; ACM: Portland OR USA, 2023; pp 173−176.

(32) Hassan Zaidi, S. S.; Sigdel, S.; Sorensen, C. M.; Kwon, G.; Li, X. Incorporation of Novel Graphene Nanosheet Materials as Cathode Catalysts in Li−O_2 Battery. *J. Electrochem. Energy Convers. Storage* **2023**, *20* (2), No. 020907.

(33) Khattab, I. S.; Bandarkar, F.; Fakhree, M. A. A.; Jouyban, A. Density, Viscosity, and Surface Tension of Water + Ethanol Mixtures From 293 to 323 K. *Korean J. Chem. Eng.* **2012**, *29* (6), 812−817.

(34) Landesfeind, J.; Hattendorff, J.; Ehrl, A.; Wall, W. A.; Gasteiger, H. A. Tortuosity Determination of Battery Electrodes and Separators by Impedance Spectroscopy. *J. Electrochem. Soc.* **2016**, *163* (7), A1373−A1387.

(35) Korchagin, O. V.; Bogdanovskaya, V. A.; Tripachev, O. V. Evaluation of Components of Li-O_2 Battery Positive Electrode Capacitance by a Voltammetric Method. *J. Electroanal. Chem.* **2022**, *920*, No. 116547.

(36) Zhao, Z.; Huang, J.; Peng, Z. Achilles' Heel of Lithium−Air Batteries: Lithium Carbonate. *Angew. Chem. Int. Ed.* **2018**, *57* (15), 3874−3886.

(37) An, Y.; Fei, H.; Zeng, G.; Ci, L.; Xiong, S.; Feng, J.; Qian, Y. Green, Scalable, and Controllable Fabrication of Nanoporous Silicon From Commercial Alloy Precursors for High-Energy Lithium-Ion Batteries. *ACS Nano* **2018**, *12* (5), 4993−5002.

(38) Morasch, R.; Keilhofer, J.; Gasteiger, H. A.; Suthar, B. Methods—Understanding Porous Electrode Impedance and the Implications for the Impedance Analysis of Li-Ion Battery Electrodes. *J. Electrochem. Soc.* **2021**, *168* (8), No. 080519.

(39) Korchagin, O. V.; Bogdanovskaya, V. A.; Tripachev, O. V. Changes in Double Layer Capacitance of the Positive Electrode in Li-O_2 Battery During Discharge: Effect of Active Material and Aprotic Electrolyte Solvent. *J. Electroanal. Chem.* **2023**, *948*, No. 117815.